ACS Synthetic Biology

pubs.acs.org/synthbio
Research Article

Quantitative Measurement of Molecular Permeability to a Synthetic Bacterial Microcompartment Shell System

Published as part of ACS Synthetic Biology special issue "Quantitative Synthetic Biology".

Eric J. Young, Henning Kirst, Matthew E. Dwyer, Josh V. Vermaas,* and Cheryl A. Kerfeld*

Cite This: ACS Synth. Biol. 2025, 14, 1405−1413
Read Online

ABSTRACT: Naturally evolved and synthetically designed forms of compartmentalization benefit encapsulated function by increasing local concentrations of substrates and protecting cargo from destabilizing environments and inhibitors. Crucial to understanding the fundamental principles of compartmentalization are experimental systems enabling the measurement of the permeability rates of small molecules. Here, we report the experimental measurement of the small-molecule permeability of a 40 nm icosahedral bacterial microcompartment shell. This was accomplished by heterologous loading of light-producing luciferase enzymes and kinetic measurement of luminescence using stopped-flow spectrophotometry. Compared to free enzyme, the luminescence signal kinetics was slower when the luciferase was encapsulated in bacterial microcompartment shells. The results indicate that substrates and products can still exchange across the shell, and modeling of the experimental data suggest that a 50× permeability rate increase occurs when shell vertices were vacant. Overall, our results suggest design considerations for the construction of heterologous bacterial microcompartment shell systems and compartmentalized function at the nanoscale.

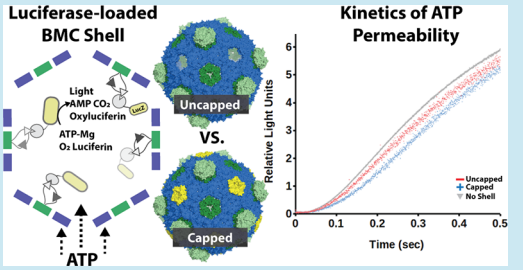

KEYWORDS: *compartmentalization, synthetic biology, biophysics, modeling, molecular permeability, ATP*

INTRODUCTION

Compartmentalization is a fundamental characteristic of life. In eukaryotes, compartment membranes are lipid-based. In contrast, in bacteria, entirely protein-based organelles known as bacterial microcompartments (BMCs) are widespread.[1,2] The "membranes" of BMCs are composed from two protein domain families: pfam00936 and pfam03319.[1,3,4] BMC-Hexamer (BMC-H) proteins contain a single pfam00936 domain and form hexagonal tiles.[5] BMC-Trimer (BMC-T) proteins consist of a tandem fusion of pfam00936 domains[6] and also form hexagonal tiles. These tiles form the facets of a polyhedral shell.[4,7−14] Pentamers that cap the vertices of the shell are formed by BMC-Pentamer (BMC-P) proteins that contain a single pfam03319 domain.[15] It is hypothesized that the spatial proximity of enzymes in the BMC lumen in conjunction with surrounding shell proteins benefits pathways via enzyme and substrate colocalization in a defined volume, by diminishing cross-talk with metabolism in the bulk cytosol, while confining toxic intermediates within the BMC.[1,16] The selective permeability properties of a BMC shell are assumed to play an essential role in supporting these benefits.

Routes for molecules to cross BMC shells are hypothesized to include shell tile compositional changes,[17,18] travel through a shell protein's centrally located pore,[5] and/or shell leakiness.[5] Simulations and structures of BMC shell proteins support that BMC shell protein pores act as a conduit for metabolites and cofactor-sized molecules.[5,6,19−24] Also, *in vivo* or *in vitro* characterized BMCs with amino acid substitutions of pore lining residues in shell proteins, or removal of the shell proteins entirely, qualitatively suggest that pore structure (and the shell itself) influences molecular permeability.[25−37] Another way BMC permeability appears modifiable is by altering the complement of shell proteins in the shell at a particular life cycle or environmental cues.[38−41] Indeed, study of a synthetic BMC shell system with programmed loading of a permeability probe supported that larger molecular cargos (∼40 Å diameter) enter shells when BMC-P vertices of a shell are deliberately left "uncapped".[42] When BMC shells are intact and capped, studies with fluorescent small molecules suggest that a shell's lumen is still chemically accessible to ∼10 Å-diameter molecules.[42,43] This supports the proposal that shell protein pores (and/or other nonspecific pathways) likely dictate molecular permeability properties of a shell. High-resolution data sets are still needed to characterize the extent to which a BMC shell acts as a diffusion barrier for small molecules. These

Received: April 24, 2024
Revised: November 15, 2024
Accepted: November 26, 2024
Published: January 14, 2025

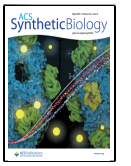

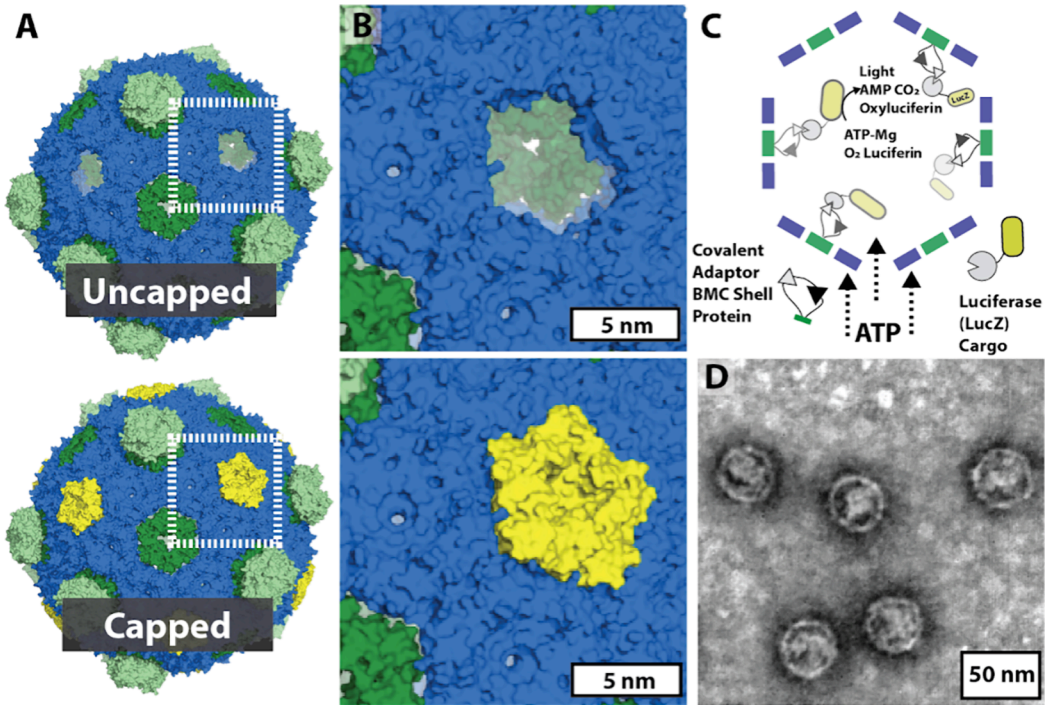

Figure 1. Design for evaluating the ATP permeability of a model BMC shell. (A) BMC shells lacking pentamers contain ∼5 nm vertex gaps (i.e., "uncapped" configuration). BMC shell structures were prepared in PyMol from PDB structure 5V74. BMC-H proteins are colored blue, BMC-T1 dark green, BMC-T2 and BMC-T3 light green, and BMC-P yellow. (B) Zoom of area bounded in white in Figure 1A. (C) Fusion of a SpyTag/SnoopTag to BMC-T1 shell protein allows for covalent tethering of reciprocally tagged-catcher cargos to the lumen of the BMC shell to evaluate the permeability of ATP to a BMC shell. (D) Transmission electron microscopy of purified uncapped LucZ-SpyCatcher BMC shells.

insights are necessary to improve fundamental understanding of BMCs in microbiomes, pathogenesis, and carbon cycling and to advance BMC shells as bionanotechnologies.

Accordingly, we designed a strategy in which lumen-localized cargo generates an output directly coupled to the molecular permeability of the shell. Numerous researchers have successfully incorporated active non-native enzymatic cargo into a BMC shell lumen.[8,44−51] Here, we heterologously load a programmable BMC shell[4,42,52,53] with firefly luciferase to act as a permeability reporter for the small-molecule adenosine triphosphate (ATP). The system relies on the *in vivo* loading of this versatile, well-characterized luminescent cargo[54,55] into a shell's lumen with the SpyTag/SpyCatcher split-adhesion covalent targeting system.[42,56] Luminescence-producing shells lacking vertices were purified and compared to counterpart shell samples with all vertices occupied (Figure 1). Stopped-flow spectrophotometry of the kinetics of light-production measured slower rising of the luminescence signal in shells in the capped versus uncapped configuration. Differential equation modeling of the experimental data revealed that capped shells are ∼50 times less permeable. Notably, these data are consistent with polar small-molecule exchange with a shell's lumen. Our approach is broadly applicable to other shell systems where it can be used to characterize engineered BMC shells and, more broadly, to uncover fundamental design principles of compartmentalization at the nanoscale.

RESULTS

Characterization of Firefly Luciferase-Loaded BMC Shells. A previously published *Haliangium ochraceum* synthetic uncapped BMC shell with a BMC-T1 SpyTag001/SnoopTag loop insertion was selected as our starting BMC shell chassis to engineer a reporter enzyme system for ATP shell permeability (Figure 1).[46] The StrepII-tagged BMC-H shell protein in the synthetic BMC shell protein operon enables purifying shells with shell BMC-P vertex vacancies (i.e., an uncapped configuration). The size of the vertex gaps is ∼5 nm in diameter. Vacancies at the vertices can be capped by adding exogenous purified BMC-P to the solution.[4,42] The type and number of oligomer shell proteins in this shell are 60 hexamers and 20 trimers in the facets, and 12 pentamers at the vertices.[4] *In vivo* coexpression of this operon with reciprocally tagged "catcher" cargos can covalently load the lumen of BMC shells.[46] We coexpressed this BMC shell operon *in vivo* with alternative N- and C-terminal SpyCatcher fusions to*Nipponoluciola cruciata* firefly luciferase (LucZ), which has been developed into a versatile bioluminescent reporter system (Figures S1−S3).[54,55] Following shell purification and anion-exchange chromatography to remove broken shell impurities, both fusion orientations contained ∼40 nm shell-sized particles measured by dynamic light scattering (DLS) (Figures S1 and S2). However, the LucZ-SpyCatcher C-terminal fusion orientation was approximately twofold higher in total luminescence (Figure S3). An activity assay of 100 μg of BMC shells loaded with LucZ-SpyCatcher detected as low as 0.5 nM of ATP in solution under our assay conditions (Figure S4).

Measuring ATP Permeability through a BMC Shell. Luminescence produced from the covalently bound lumen-located LucZ-SpyCatcher serves as a reporter for permeability of the shell to ATP. In this system, LucZ is confined to the BMC lumen by the covalent tether and is not anticipated to exchange with the bulk outside the shell lumen. LucZ uses

https://doi.org/10.1021/acssynbio.4c00290
ACS Synth. Biol. 2025, 14, 1405−1413

ATP, luciferin, and oxygen to generate visible light, so luminescence activity supports substrates crossing the BMC shell, and therefore, any change in the kinetics of luminescence implies an altered permeability rate. LucZ-containing shell samples had ∼100 nM final concentration of protein in solution, while purified BMC-P was added to a second sample at up to 10 molar excess of shells in solution (Figure S5). At this ratio, it is expected that shell vertices are fully capped and do not permit passage of molecules larger than the shell's pores.[42] After incubation in a luciferin and $MgCl_2$-containing buffer at room temperature for at least 16 h, DLS, negative staining and transmission electron microscopy (TEM), and a luminescence assay in the presence of ATP indicated the preservation of shell size, structure, and luciferase activity (Figure S6).

Reaction kinetics were then measured with stopped-flow spectrophotometry (Figure 2 and Figures S7−S9). BMC shell

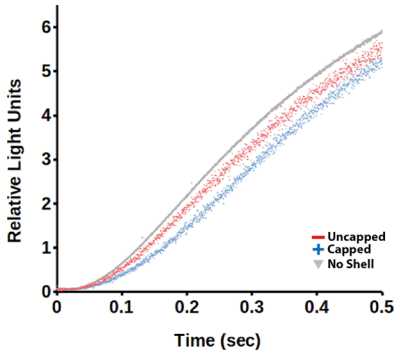

Figure 2. Measuring ATP permeability of LucZ-SpyCatcher BMC shells with stopped-flow assays. (A) Stopped-flow assay comparison of uncapped versus capped shells versus a shell-free LucZ in a luciferin/$MgCl_2$ substrate (each trace represents five readings averaged to one). The concentration of shell samples in solution was 100 nM, while the No Shell sample was 1000 nM. Samples were incubated for 1 h in 1 mM luciferin/$MgCl_2$, 50 mM Tris−HCl, and 200 mM NaCl pH 8.0 buffer with or without 1000 nM BMC-P capping protein. Trends represented are from at least three independent experiments.

samples preincubated in the substrate buffer were placed in one injection syringe, while a solution of ATP in the buffer was placed in the other injection syringe. Upon mixing, a rise in luminescence in both capped and uncapped shells occurred, which peaked after approximately 1 s. Notably, the uncapped shell samples' luminescence signal intensity reproducibly rose with a steeper slope than the capped shell sample. We then affinity purified a "No Shell" His-LucZ-SpyCatcher control and compared the kinetics of luminescence production with His-LucZ-SpyCatcher covalently tethered inside via SpyTag in uncapped or capped shells (Figure 2 and Figure S7C). When the No Shell control in the substrate buffer is injected, this sample has faster kinetics than both the uncapped and capped samples. A concentration of 1000 nM for the No Shell control was used in order to account for any viscosity changes due to surplus (i.e., unincorporated in shells) protein in solution because this is the concentration of pentamer in solution in capped samples. Averaging three independent biological replicates support distinct trendline equations and a statistical difference among all samples (p value <0.05) (Figure S7C). We also performed a control experiment by adding a molecular crowder to intentionally delay luminescence due to an increase in solution viscosity, decreasing Brownian diffusion rates of molecules in the system. This occurred and with similarity to previously reported trends: luminescence rose fastest in the shell-lacking control followed by uncapped and then capped samples (Figure S8). An exception is the No Shell control in 20% PEG, which appears to unexpectedly slow more than the 10% PEG and buffer-only samples. We note that this sample routinely had aggregates visible to the eye, hinting that these samples without a shell were not as stable under the 20% PEG6000 condition. We also tested the influence of varying the concentration of capping pentamer (Figure S9). To avoid the influence of viscosity changes due to excess pentamer in solution, we incubated shells with pentamer overnight in Luciferin/$MgCl_2$ substrate buffer and then removed pentamers by anion-exchange chromatography and a 100 kDa cutoff Amicon filter, which retains shells, while free pentamer collects in the filtrate. Overall, as observed in Figure S9, shells lacking a capping pentamer have the fastest kinetics, while shells with a 1:10 substoichiometric amount of pentamer have intermediate kinetics between an uncapped versus full-capped system and samples with excess pentamer have the slowest kinetics.

To determine the overall effect of encapsulation on enzymatic activity, we calculated the Km* for ATP, its binding affinity for the encapsulated luciferase. We term this quantity Km* to avoid confusion with the Km intrinsic to luciferase in a freely diffusing system without confinement, which is approximately 15 μM.[57] We found that Km* ATP for capped samples was approximately eightfold higher (∼16 μM ATP for uncapped versus ∼119 μM ATP for capped) (Figure S10). This further strengthens the notion that BMC shells provide a diffusion barrier to ATP, but they are not fully impermeable to it. In particular, the similarity of Km between uncapped systems with free luciferase highlights the greatly accelerated kinetics for uncapped systems.

As shown in Figure 2, it is clear that the uncapped BMC shells are more permeable than the capped shells because of the increase of the LucZ's kinetic rate in the uncapped samples. Intuitively, the absence of the 12 pentameric vertices of the shell icosahedron provides an opening through which small molecules can permeate more freely, whereas small molecules that encounter capped shells have a higher probability of being reflected back into solution rather than entering the shell. Turning this qualitative picture into a quantitative model depends on the selection of a model itself. Because the general luminescence pattern is similar for enzymes in bulk solution and samples containing enzymes tethered within a shell (with an initial nonlinear rise followed by a peak and a nonlinear decline in luminance), multiple models were tested. The model that fits best under all conditions is one in which intermediate products inhibit enzyme activity in a two-step reaction.[54,55] The selected model also agrees best with the established luciferase reaction mechanism of ATP first reacting with D-luciferin to D-luciferyl-AMP and PPi; D-luciferyl-AMP is then converted to oxyluciferin and AMP upon O_2 reacting, releasing light and CO_2.[57] The formal differential equations solved numerically are derived in the Supporting Information. The differential equations can be fit either for an individual trace or instead use a shared set of thermodynamic and kinetic parameters with varying initial concentrations.

We aggregated comparable data sets together to create a unified fit (Table S2). Figure 3 summarizes the key findings of this analysis, including the permeability coefficient Px, which is a measure for how much the BMC shell represents a diffusion barrier to the rate-limiting substrate. While this substrate could

https://doi.org/10.1021/acssynbio.4c00290
ACS Synth. Biol. 2025, 14, 1405−1413

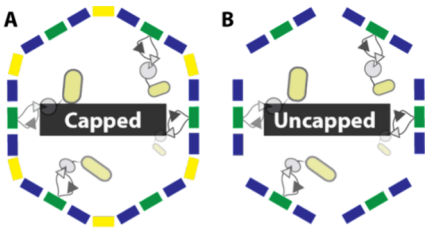

Permeability	
Px (nm/s)	114
Py (nm/s)	1.26

Permeability	
Px (nm/s)	5,280
Py (nm/s)	58.3

Figure 3. Differential equation modeling of stop-flow enzyme kinetics to calculate the permeability rate of capped versus uncapped shells. (A, B) Permeability coefficients are given by the rate of the limiting substrate (Px) and the rate of the intermediate complex (Py). Information regarding the equations, assumptions, and additional calculated values is found in the Supporting Information. (A) Capped shells. (B) Uncapped shells.

be ATP, luciferin, or O_2, it is likely that it is ATP, as it is the largest substrate molecule and it was absent initially in the samples in the stopped-flow measurements. Py is the permeability coefficient for the intermediate D-luciferyl-AMP. Py is much smaller than Px, indicating that the BMC shell permits influx for the limiting reactant about two orders of magnitude greater than an efflux of the intermediate D-luciferyl-AMP. As can be seen from the data in Table S3, the kinetic parameters appear sensitive to solution conditions. However, as the trends in fit parameters are not consistent as the PEG concentration is increased, our interpretation is that the parameters are simply difficult to fit consistently. We see this in evidence again in quantities like the acceleration factor of capped and uncapped shell permeabilities, which is effectively unchanged across solution conditions when the buffer parameters are used to seed the parameters under other solution conditions (Table S3). Once one solution is found, our fitting routines have great difficulty finding dramatically different solutions to the differential equations. Fitting caveats aside, we see that smaller molecules (ATP or luciferin) permeate more quickly than the larger D-luciferyl-AMP intermediate product and that uncapped shells have faster permeation overall compared to capped shells. The permeability rates calculated appear congruent with stop-flow kinetic measurements (Figure 2) that qualitatively suggested differences to shell permeability: the luminescence response is fastest without a shell, and then if the shell is uncapped, and finally if a shell is capped, representing a growing barrier to molecular access to the shell's interior with enzymes.

Within our model, we assumed that uncapped shell permeation was a consistent multiplicative factor higher than the capped shell permeability coefficient. As the model evolved, and depending on how much data was considered during fitting, this value ranged from around 50 to up to 10,000. The unified fit accounting for as much data as possible supports estimates at the lower end of that range, but we again highlight the uncertainty that is possible. A 50× acceleration may, however, be the most plausible. The pentameric vertices account for only about 7% of the total surface area of an intact 40 nm shell. If this shell reflects about 1200 molecules back into solution for each molecule that permeates, as recently estimated for other small molecules using direct simulation,[24] a molecule that hits the uncovered 7% of the total surface area would be about 1200 times more likely to permeate through that uncapped space. This simple model implies that the overall rate of permeation would increase by about a factor of 85 in uncapped shells (1200 × 0.07), which is reasonably close to the 50× rate enhancement determined from the fit.

DISCUSSION

Our measured values for a BMC shell's permeability (ranging from 10^{-7} to 10^{-4} cm/s) appear similar in magnitude to permeability values observed for passive transport of small molecules across lipid bilayers[58] but are considerably smaller than the 10^{-2} cm/s permeabilities for small photosynthetic metabolites through a synthetic carboxysome shell.[24] Yet, previous descriptions of BMC shell permeability using mathematical modeling approximate a similar order of magnitude for small-molecule permeability as reported here.[59−61] The protein composition of shells, their overall size as well as small-molecule substrates and products, and interior cargo density all likely influence a BMC shell's permeability. We anticipate that many of the same molecular permeability principles at play in lipid membrane-bound compartments may also apply to BMC shells in both native and engineered examples.[62]

For instance, at a steady state, the flux across the shell must be identical to catalytic turnover for any encapsulated enzymes such as the LucZ trapped here. This means that the number of enzyme turnovers is bounded from above by the inbound flux, which is related to the concentration difference and the permeability (flux = permeability × surface area × ΔC). As a corollary, the concentration inside the shell must be less than the concentration outside the shell in order for substrates to diffuse into a BMC down a concentration gradient. As a result, catalysis is always slower when a barrier is present with one enzyme reaction, such as the LucZ system constructed here. This concept appears clear when comparing between capped, uncapped, and no shell conditions (Figure 2), as luminescence increases fastest when no shell is present. Considering that we can measure luciferase activity encapsulated within a BMC shell over many minutes, it is very likely that not only ATP but also luciferin and O_2 are able to cross the shell, as these substrates would otherwise be quickly exhausted inside the 40 nm compartment. The permeability coefficients of the limiting reactant (ATP or luciferin) and D-luciferyl-AMP across the BMC shell are roughly two orders of magnitude apart (Table S3). These differences may be explained by differences in the molecular size and/or charge of the molecules, indicating that larger and more negatively charged molecules diffuse at a slower rate across a BMC shell.

It is instructive to quantify the molecular fluxes that might be present. For the LucZ system, we can assume a kcat of approximately 1 s^{-1}, based on single-digit kcat reported in the literature.[63,64] In the BMC shells designed here, where the luciferase is tethered onto functionalized trimer protomers, at most, there could be 20 LucZ enzymes present. In practice, approximately 30% of the trimers are thought to be bound to LucZ in the SpyTag/SpyCatcher system, and so we assume for this discussion that five LucZ enzymes are actually in the interior of the shell, turning over 5 s^{-1} at maximum. Based on the permeabilities we determined and the surface area for the shell, the concentration difference that would saturate the encapsulated enzymes is only 320 μmol/L. Accordingly, we

https://doi.org/10.1021/acssynbio.4c00290
ACS Synth. Biol. 2025, 14, 1405−1413

would expect just a 320 μmol/L concentration difference created by the enzymatic activity inside a shell. Since the concentration outside the shell is much higher in our conditions (in the mmol/L range), the concentration inside versus outside the BMC shell is difficult to distinguish in our stopped-flow experiments. If we use the uncapped permeability, which is ∼50 times larger, the concentration difference required to saturate the encapsulated enzymes would be 50× smaller.

Under what circumstances might the increased permeability of uncapped shells be advantageous? For single enzyme reactions, uncapping the shells lowers the concentration difference between inside and outside the shell, potentially accelerating the kinetics for enzymes that are diffusion limited. We also envision scenarios where catalysis is accelerated by uncapping the shell if a product or reactant is too large to fit through a sealed BMC shell. For multienzyme pathways encapsulated within a single BMC, the increased permeability associated with an uncapped shell may be detrimental to the overall catalytic efficiency, as the built-up concentration of the product for the first reaction could escape through the vertex gaps in the shell. If, however, the gaps make up a significantly smaller percentage of the surface area of the BMC shell (such as in larger BMCs similar in size to beta-carboxysomes), the impact of reactants slipping away would be reduced. Additionally, as shown in Figure S9, BMC shells can also exist in incomplete capping states that have reaction kinetics intermediate to an uncapped or capped system. Incomplete capping opens the possibility for larger substrates, repair enzymes, or chaperones to exchange across the shell, while the activity reduction from small molecules diffusing out of the shell is minimized.

Accordingly, sealed shells appear to cater best to multistep pathways. When encapsulating a multistep pathway, any step after the first one will theoretically have higher enzymatic activity as the intermediate concentrations will be higher inside than outside. Thus, the overall performance of a metabolic pathway may increase for particularly slow enzymes requiring a high substrate concentration to work efficiently as long as the enzymatic step before is also encapsulated and not significantly impacted by the BMC shell diffusion barrier. Regarding this barrier, in general, the first substrate should be able to diffuse inward as freely as possible to not negatively impact the first catalytic step. However, retention of intermediates formed during reaction should remain inside to benefit downstream enzymatic reactions—this requires the BMC shell to represent a large diffusion barrier in this instance. In fact, this suggested design principle appears to be observed in the case for BMCs called carboxysomes. These systems encapsulate the catalytically fast carbonic anhydrase delivering the intermediate CO_2 to notoriously catalytically slow and error prone enzyme RuBisCO.[17] Because both the permeability properties of the BMC shell toward the first substrate and downstream intermediates might not be completely independently engineerable, compromise appears necessary.

BMCs occur in nearly 70 different varieties of cargo-containing cores and are theoretically built from compositions of nearly 40,000 unique shell proteins.[2,65] Research suggests that cyanobacterial carboxysomes alter compositions of a BMC shell under environmental change, and it is hypothesized that these alterations regulate molecular permeability.[38,40,41] The detailed influence of a BMC's specific shell protein composition on permeability (versus a dramatic global composition alteration as here, by completely omitting pentamer to create vertex vacancies) remains to be quantitatively experimentally measured. Growth in computing power continues to push the resolution and time scale at which BMC shells are simulated, even in the presence of metabolites and enzymatic cargos.[24]

More broadly, engineering molecular permeability reporters inside BMC shell systems will enable the design−build−test−learn cycle of engineering custom nanoreactors built from BMC shells. Of consideration in this effort is our approximately eightfold measured change from reported literature of LucZ Km for ATP when in the capped configuration.[57] This supports altering a shell's small-molecule permeability rate by including capping pentamers, which is an important design consideration for how molecularly crowded, subdiffusive environments impact enzyme activity and/or kinetics.[66,67] Additionally, in this effort to describe shell permeability, we observed in crowded conditions that encapsulation within a shell reduced activity loss compared to the enzymes free in solution. This suggests another way in which enzymatic compartmentalization and/or scaffolding improves an enzyme's resilience in crowded and destabilizing environments.[68]

MATERIALS AND METHODS

Molecular Biology, Cell Growth, and Protein Purification. Plasmids were constructed with isothermal DNA assembly from purchased synthetic DNA (IDT) and PCR-amplified genes. Table S3 lists the plasmids used in this study. ∼50 ng of shell and LucZ cargo plasmids were cotransformed into*Escherichia coli* BL21 T7 Express (NEB) and placed on double-resistance LB antibiotic plates. A single colony was grown in 100 mL of antibiotic-supplemented LB. A 1:100 dilution of the overnight culture-seeded 1 L cultures for protein purification. After growth at 37 °C until OD600 0.8, a 20 min ice incubation cooled the cultures and then 100 μM IPTG and 50 ng/μL ATc were added to induce protein production. Growth proceeded overnight at 24 °C. 4500 × *g* centrifugation at 4 °C was used to harvest the cells from the LB, and a French press (∼1250 PSI) (in the presence of a pinch lysozyme, 6 μL of Dr. Nuclease, and ∼3 mg of DNAase per 20 g of cell paste) was used to rupture samples in a 50 mM Tris−HCl, 200 mM NaCl pH 8.0 buffer. Lysates were clarified at 27,000 × *g* for 30 min. Lysates were stacked on top of a 30% sucrose layer in lysis buffer, and ultracentrifugation at 40,000 rpm in a 70Ti rotor for a minimum of 16 h at 4 °C separated shells from other cellular materials. Glassy ultracentrifugation pellets were resuspended in lysis buffer, mixed until particles dissolved, centrifuged at 14,000 × *g* for 5 min to remove insoluble matter, and then applied to a 5 mL StrepTrap HP column pre-equilibrated in cold lysis buffer with a syringe pump. Five column volumes of cold lysis buffer were applied to wash away nonspecifically bound molecules. Two or three column volumes of 20 mM Tris−HCl, 50 mM NaCl, pH 8.0 buffer, and 2.5 mM D-thiobiotin were applied to elute the sample. The eluant was centrifuged at 14,000 × *g* for 5 min at 4 °C and applied with SuperLoop to a 5 mL MonoQ 10/100 GL column at 3 mL/min in 20 mM Tris−HCl, 50 mM NaCl, pH 8.0. A gradient with applied 20 mM Tris−HCl, 1000 mM NaCl, pH 8.0, and approximately 35−40% high salt fractions was pooled. 4200 × *g* centrifugation through a 100 kDa Amicon ultrafilter was performed to concentrate samples and exchange shells to the lysis buffer. Sample protein purity was

https://doi.org/10.1021/acssynbio.4c00290
ACS Synth. Biol. 2025, 14, 1405−1413

analyzed by 20% SDS-PAGE gels. Samples were stored at 4 °C with 0.01% sodium azide added as a preservative. Luciferase activity and shell sample monodispersity were stable for months in this solution (data not shown).

Luminescence Measurement of Luciferase Reaction. The protein concentration was measured using a NanoDrop UV−vis instrument (Thermo Fisher) in E1% mode. A specified microgram of protein was added to a black skirted and nontreated 96-well plate (Thermo Fisher). Final reaction volumes were 100−200 μL of lysis buffer with a final concentration of 1 mM luciferin, and 1 mM $MgCl_2$ in the reaction was used. A Tecan Spark microplate reader in luminescence mode was used to measure the luciferase reaction. A specified concentration of ATP either was manually added with a pipet or injected using the Tecan Spark Injector module. Luminescence was recorded with 100 ms integration time and three measurements with 2 s delays per well.

Dynamic Light Scattering. A Wyatt DynaPro NanoStar DLS was employed to measure protein size in solution. Before measurement, samples were adjusted to 1 mg·mL and centrifuged for 14,000 × *g* for 5 min. A 4 μL sample was loaded in the quartz cuvette, and data was collected with an acquisition time of 4 s for 25 measurements each per sample with three technical replicates in total. Measurements were individually filtered for a baseline value of >1.0 and a sum of squares value of <35.0.

Transmission Electron Microscopy. Purified samples at 1 mg/mL were diluted to 0.2 mg/mL in water, and a 5 μL drop was applied to a 150-mesh copper grid (Electron Microscopy Sciences, Hatfield, USA) on parafilm for 30 s. The drop was gently wicked away and stained with a 5 μL droplet of 1% uranyl acetate for 15 s (negative stain). Excess uranyl acetate liquid was gently wicked away. Grids were imaged on a JEM-1400Flash (JEOL, Nieuw-Vennep, Tokyo) TEM at an accelerating voltage of 100 kV.

Stopped-Flow Spectrophotometry. An Applied Photophysics SX20 stopped-flow spectrophotometer was used to record shells containing luciferase kinetics. Fluorescence mode on the SX20 was used, but the light source was left off for these reactions in order to collect the light produced by the luciferase reaction. After washing the syringes and driving lysis buffer through the mixing chamber, the sample size was set to 10,000 and individual sample syringes were loaded with room-temperature solutions. Inlet A contained the solution of shells preincubated with $MgCl_2$ and luciferin substrate in lysis buffer, while inlet B contained the indicated concentration of ATP in lysis buffer. A collection time period was set (between 0.125 and 60 s), and the drive volume was estimated at 40 μL per syringe. After 10 manual drives to flush the system with a sample, the kinetic spectrum was acquired. Each acquisition obtained five kinetic trace measurements. These traces were then averaged with Pro-Data Viewer SX20 software and exported as a CSV file.

Data Analysis and Figure Preparation. OpenOffice Calc (Apache) was used to organize the data and prepare the graphs. The GNU Image Manipulation Program (The GIMP Development Team) and FIJI[69] were used to adjust the brightness and contrast of images. PyMol (The PyMOL Molecular Graphics System, Version 3.0 Schrödinger, LLC) was employed to create protein representations. The ColabFold server using AlphaFold2 was used to create the Luciferase and SpyCatcher fusion protein structural models.[70] Adobe Illustrator (Adobe Inc.) was used to construct the figure panels. Km calculations of uncapped and capped shell samples were calculated by using Pro-Data Viewer SX20 software's equation fitting function to first determine initial rates of the exponential phase of luminescence kinetics. Rate constants were then plotted against substrate concentration and fitted to a linear regression where the slope was equal, Km/K_2.

Permeability Calculations. A set of coupled differential equations was devised as a model to represent how concentrations vary as a function of time, with the complete derivation presented in the Supporting Information. The coupled differential equations that result are similar to prior work by Dale et al.[54,55] The coupled differential equations were solved numerically through the odefit routine in SciPy.[71] The residual between the solution to the differential equation and the measured luminances from stopped-flow calculations were minimized using the default Levenberg−Marquardt least-squares algorithm implemented in lmfit version 1.2.2 (https://zenodo.org/doi/10.5281/zenodo.598352.[72] The permeabilities are model parameters and are read directly from the parameters that minimize the residuals. The code to parse the measured luminescence and implement the fit is available from Github (DOI: 10.5281/zenodo.10963263).

■ ASSOCIATED CONTENT

Supporting Information

The Supporting Information is available free of charge at https://pubs.acs.org/doi/10.1021/acssynbio.4c00290.

Purification of in vivo covalently loaded SpyCatcher-LucZ-uncapped BMC shells; purification of in vivo covalently loaded LucZ-SpyCatcher-uncapped BMC shells; luminescence activity comparison between LucZ and SpyCatcher fusion orientation; activity assay of His-LucZ-SpyCatcher-loaded uncapped BMC shells; capping pentamer protein purification, and workflow for comparing shell permeability in uncapped versus capped configuration; LucZ-SpyCatcher Shells after incubation in substrate buffer; stopped-flow spectrophotometry of uncapped and capped BMC shells; stopped-flow spectrophotometry of uncapped and capped shells in 10 and 20% PEG6000 buffer; stopped-flow spectrophotometry of MonoQ-purified shells after capping; calculation of kM of uncapped and capped LucZ-SpyCatcher BMC shells; protein expression vectors; coding sequences of expression vectors; differential equations for luciferase activity without shells; and addition of permeability into the model (PDF)

Accession Codes

The code for the fitting, and reading in the experimental data, is provided on github (DOI: 10.5281/zenodo.10963263).

■ AUTHOR INFORMATION

Corresponding Authors

Josh V. Vermaas − *MSU-DOE Plant Research Laboratory and Biochemistry and Molecular Biology Department, Michigan State University, East Lansing, Michigan 48824, United States;* orcid.org/0000-0003-3139-6469; Email: vermaasj@msu.edu

Cheryl A. Kerfeld − *Environmental Genomics and Systems Biology Division, Lawrence Berkeley National Laboratory, Berkeley, California 94702, United States; MSU-DOE Plant Research Laboratory and Biochemistry and Molecular Biology Department, Michigan State University, East*

Lansing, Michigan 48824, United States; Molecular Biophysics and Integrated Bioimaging Division, Lawrence Berkeley National Laboratory, Berkeley, California 94702, United States; orcid.org/0000-0002-9977-8482; Email: ckerfeld@lbl.gov

Authors

Eric J. Young − *Environmental Genomics and Systems Biology Division, Lawrence Berkeley National Laboratory, Berkeley, California 94702, United States;* orcid.org/0000-0002-6770-6310

Henning Kirst − *Environmental Genomics and Systems Biology Division, Lawrence Berkeley National Laboratory, Berkeley, California 94702, United States; Departamento de Genética, Campus de Excelencia Internacional Agroalimentario ceiA3, Universidad de Córdoba, Córdoba 14071, Spain; Instituto Maimónides de Investigación Biomédica de Córdoba (IMIBIC), Córdoba 14004, Spain*

Matthew E. Dwyer − *MSU-DOE Plant Research Laboratory, Michigan State University, East Lansing, Michigan 48824, United States;* orcid.org/0000-0002-0690-564X

Complete contact information is available at: https://pubs.acs.org/10.1021/acssynbio.4c00290

Author Contributions

E.J.Y. designed the experiments, collected data, and led the manuscript drafting. H.K. designed the experiments and collected preliminary data. M.E.D generated electron microscopy data. J.V.V. developed permeability modeling approaches to fit to collected measurements. C.A.K acquired funding and designed and supervised the project. All authors contributed to manuscript writing. The authors thank Dr. John C. Steele for early contributions to experimental design.

Notes

The authors declare no competing financial interest.

■ ACKNOWLEDGMENTS

We thank the current and former members of the Kerfeld Lab for helpful discussions and initial cloning efforts. This work was supported by the National Institutes of Health, National Institute of Allergy and Infectious Diseases (NIAID), grant 5R01AI114975-08. The permeability modeling by J.V.V. was supported in part by the US Department of Energy, Basic Energy Sciences, DE-SC0023395.

■ REFERENCES

(1) Kerfeld, C. A.; Aussignargues, C.; Zarzycki, J.; Cai, F.; Sutter, M. Bacterial Microcompartments. *Nat. Rev. Microbiol.* **2018**, *16* (5), 277−290.

(2) Sutter, M.; Melnicki, M. R.; Schulz, F.; Woyke, T.; Kerfeld, C. A. A Catalog of the Diversity and Ubiquity of Bacterial Microcompartments. *Nat. Commun.* **2021**, *12* (1), 3809.

(3) Steele, J. F. C.; Kerfeld, C. *A. Encyclopedia of Biological Chemistry* **2021**, *III*, 108−122.

(4) Sutter, M.; Greber, B.; Aussignargues, C.; Kerfeld, C. A. Assembly Principles and *Structure* of a 6.5-MDa Bacterial Microcompartment Shell. *Science* **2017**, *356* (6344), 1293−1297.

(5) Kerfeld, C. A.; Sawaya, M. R.; Tanaka, S.; Nguyen, C. V.; Phillips, M.; Beeby, M.; Yeates, T. O. Protein Structures Forming the Shell of Primitive Bacterial Organelles. *Science* **2005**, *309* (5736), 936−938.

(6) Klein, M. G.; Zwart, P.; Bagby, S. C.; Cai, F.; Chisholm, S. W.; Heinhorst, S.; Cannon, G. C.; Kerfeld, C. A. Identification and Structural Analysis of a Novel Carboxysome Shell Protein with Implications for Metabolite Transport. *J. Mol. Biol.* **2009**, *392* (2), 319−333.

(7) Ferlez, B. H.; Kirst, H.; Greber, B. J.; Nogales, E.; Sutter, M.; Kerfeld, C. A. Heterologous Assembly of Pleomorphic Bacterial Microcompartment Shell Architectures Spanning the Nano- to Microscale. *Adv. Mater.* **2023**, *35* (23), No. e2212065.

(8) Tan, Y. Q.; Ali, S.; Xue, B.; Teo, W. Z.; Ling, L. H.; Go, M. K.; Lv, H.; Robinson, R. C.; Narita, A.; Yew, W. S. Structure of a Minimal A-Carboxysome-Derived Shell and Its Utility in Enzyme Stabilization. *Biomacromolecules* **2021**, *22* (10), 4095−4109.

(9) Cesle, E. E.; Filimonenko, A.; Tars, K.; Kalnins, G. Variety of Size and Form of GRM2 Bacterial Microcompartment Particles. *Protein Sci.* **2021**, *30* (5), 1035−1043.

(10) Sutter, M.; Laughlin, T. G.; Sloan, N. B.; Serwas, D.; Davies, K. M.; Kerfeld, C. A. Structure of a Synthetic *β*-Carboxysome Shell. *Plant Physiol.* **2019**, *181* (3), 1050−1058.

(11) Evans, S. L.; Al-Hazeem, M. M. J.; Mann, D.; Smetacek, N.; Beavil, A. J.; Sun, Y.; Chen, T.; Dykes, G. F.; Liu, L.-N.; Bergeron, J. R. C. Single-Particle Cryo-EM Analysis of the Shell Architecture and Internal Organization of an Intact *α*-Carboxysome. *Structure* **2023**, *31* (6), 677−688.

(12) Greber, B. J.; Sutter, M.; Kerfeld, C. A. The Plasticity of Molecular Interactions Governs Bacterial Microcompartment Shell Assembly. *Structure* **2019**, *27* (5), 749−763.

(13) Zhou, R.-Q.; Jiang, Y.-L.; Li, H.; Hou, P.; Kong, W.-W.; Deng, J.-X.; Chen, Y.; Zhou, C.-Z.; Zeng, Q. Structure and Assembly of the *α*-Carboxysome in the Marine Cyanobacterium Prochlorococcus. *Nat. Plants* **2024**, *10*, 661−672.

(14) Ni, T.; Jiang, Q.; Ng, P. C.; Shen, J.; Dou, H.; Zhu, Y.; Radecke, J.; Dykes, G. F.; Huang, F.; Liu, L.-N.; Zhang, P. Intrinsically Disordered CsoS2 Acts as a General Molecular Thread for *α*-Carboxysome Shell Assembly. *Nat. Commun.* **2023**, *14* (1), 5512.

(15) Tanaka, S.; Kerfeld, C. A.; Sawaya, M. R.; Cai, F.; Heinhorst, S.; Cannon, G. C.; Yeates, T. O. Atomic-Level Models of the Bacterial Carboxysome Shell. *Science* **2008**, *319* (5866), 1083−1086.

(16) Kerfeld, C. A.; Erbilgin, O. Bacterial Microcompartments and the Modular Construction of Microbial Metabolism. *Trends Microbiol.* **2015**, *23* (1), 22−34.

(17) Liu, L.-N. Advances in the Bacterial Organelles for CO2 Fixation. *Trends Microbiol.* **2022**, *30* (6), 567−580.

(18) Turmo, A.; Gonzalez-Esquer, C. R.; Kerfeld, C. A. Carboxysomes: Metabolic Modules for CO2 Fixation. *FEMS Microbiol. Lett.* **2017**, *364* (18), 1000118.

(19) Faulkner, M.; Szabó, I.; Weetman, S. L.; Sicard, F.; Huber, R. G.; Bond, P. J.; Rosta, E.; Liu, L.-N. Molecular Simulations Unravel the Molecular Principles That Mediate Selective Permeability of Carboxysome Shell Protein. *Sci. Rep.* **2020**, *10* (1), 17501.

(20) Tsai, Y.; Sawaya, M. R.; Cannon, G. C.; Cai, F.; Williams, E. B.; Heinhorst, S.; Kerfeld, C. A.; Yeates, T. O. Structural Analysis of CsoS1A and the Protein Shell of the Halothiobacillus Neapolitanus Carboxysome. *PLoS Biol.* **2007**, *5* (6), No. e144.

(21) Mahinthichaichan, P.; Morris, D. M.; Wang, Y.; Jensen, G. J.; Tajkhorshid, E. Selective Permeability of Carboxysome Shell Pores to Anionic Molecules. *J. Phys. Chem. B* **2018**, *122* (39), 9110−9118.

(22) Trettel, D. S.; Neale, C.; Zhao, M.; Gnanakaran, S.; Gonzalez-Esquer, C. R. Monatomic Ions Influence Substrate Permeation across Bacterial Microcompartment Shells. *Sci. Rep.* **2023**, *13* (1), 15738.

(23) Park, J.; Chun, S.; Bobik, T. A.; Houk, K. N.; Yeates, T. O. Molecular Dynamics Simulations of Selective Metabolite Transport across the Propanediol Bacterial Microcompartment Shell. *J. Phys. Chem. B* **2017**, *121* (34), 8149−8154.

(24) Sarkar, D.; Maffeo, C.; Sutter, M.; Aksimentiev, A.; Kerfeld, C. A.; Vermaas, J. V. Atomic View of Photosynthetic Metabolite Permeability Pathways and Confinement in Synthetic Carboxysome Shells. *Proc. Natl. Acad. Sci. U. S. A.* **2024**, *121* (45), No. e2402277121.

(25) Penrod, J. T.; Roth, J. R. Conserving a Volatile Metabolite: A Role for Carboxysome-Like Organelles in Salmonella Enterica. *J. Bacteriol.* **2006**, *188* (8), 2865−2874.

(26) Havemann, G. D.; Sampson, E. M.; Bobik, T. A. PduA Is a Shell Protein of Polyhedral Organelles Involved in Coenzyme B 12 -Dependent Degradation of 1,2-Propanediol in Salmonella Enterica Serovar Typhimurium LT2. *J. Bacteriol.* **2002**, *184* (5), 1253−1261.
(27) Chowdhury, C.; Chun, S.; Pang, A.; Sawaya, M. R.; Sinha, S.; Yeates, T. O.; Bobik, T. A. Selective Molecular Transport through the Protein Shell of a Bacterial Microcompartment Organelle. *Proc. Natl. Acad. Sci. U. S. A.* **2015**, *112* (10), 2990−2995.
(28) Chowdhury, C.; Chun, S.; Sawaya, M. R.; Yeates, T. O.; Bobik, T. A. The Function of the PduJ Microcompartment Shell Protein Is Determined by the Genomic Position of Its Encoding Gene. *Mol. Microbiol.* **2016**, *101* (5), 770−783.
(29) Chowdhury, C.; Bobik, T. A. Engineering the PduT Shell Protein to Modify the Permeability of the 1,2-Propanediol Microcompartment of Salmonella. *Microbiology* **2019**, *165* (12), 1355−1364.
(30) Cai, F.; Menon, B. B.; Cannon, G. C.; Curry, K. J.; Shively, J. M.; Heinhorst, S. The Pentameric Vertex Proteins Are Necessary for the Icosahedral Carboxysome Shell to Function as a CO2 Leakage Barrier. *PLoS One* **2009**, *4* (10), No. e7521.
(31) Lee, M. F. S.; Jakobson, C. M.; Tullman-Ercek, D. Evidence for Improved Encapsulated Pathway Behavior in a Bacterial Microcompartment through Shell Protein Engineering. *ACS Synth. Biol.* **2017**, *6* (10), 1880−1891.
(32) Huang, J.; Jiang, Q.; Yang, M.; Dykes, G. F.; Weetman, S. L.; Xin, W.; He, H.-L.; Liu, L.-N. Probing the Internal PH and Permeability of a Carboxysome Shell. *Biomacromolecules* **2022**, *23* (10), 4339−4348.
(33) Rae, B. D.; Long, B. M.; Badger, M. R.; Price, G. D. Structural Determinants of the Outer Shell of β-Carboxysomes in Synechococcus Elongatus PCC 7942: Roles for CcmK2, K3-K4, CcmO, and CcmL. *PLoS One* **2012**, *7* (8), No. e43871.
(34) Cai, F.; Sutter, M.; Bernstein, S. L.; Kinney, J. N.; Kerfeld, C. A. Engineering Bacterial Microcompartment Shells: Chimeric Shell Proteins and Chimeric Carboxysome Shells. *ACS Synth. Biol.* **2015**, *4* (4), 444−453.
(35) Cameron, J. C.; Wilson, S. C.; Bernstein, S. L.; Kerfeld, C. A. Biogenesis of a Bacterial Organelle: The Carboxysome Assembly Pathway. *Cell* **2013**, *155* (5), 1131−1140.
(36) Yang, M.; Wenner, N.; Dykes, G. F.; Li, Y.; Zhu, X.; Sun, Y.; Huang, F.; Hinton, J. C. D.; Liu, L.-N. Biogenesis of a Bacterial Metabolosome for Propanediol Utilization. *Nat. Commun.* **2022**, *13* (1), 2920.
(37) Huseby, D. L.; Roth, J. R. Evidence That a Metabolic Microcompartment Contains and Recycles Private Cofactor Pools. *J. Bacteriol.* **2013**, *195* (12), 2864−2879.
(38) Sommer, M.; Sutter, M.; Gupta, S.; Kirst, H.; Turmo, A.; Lechno-Yossef, S.; Burton, R. L.; Saechao, C.; Sloan, N. B.; Cheng, X.; Chan, L.-J. G.; Petzold, C. J.; Fuentes-Cabrera, M.; Ralston, C. Y.; Kerfeld, C. A. Heterohexamers Formed by CcmK3 and CcmK4 Increase the Complexity of Beta Carboxysome Shells. *Plant Physiol.* **2019**, *179* (1), 156−167.
(39) Garcia-Alles, L. F.; Root, K.; Maveyraud, L.; Aubry, N.; Lesniewska, E.; Mourey, L.; Zenobi, R.; Truan, G. Occurrence and Stability of Hetero-Hexamer Associations Formed by β-Carboxysome CcmK Shell Components. *PLoS One* **2019**, *14* (10), No. e0223877.
(40) Sun, Y.; Wollman, A. J. M.; Huang, F.; Leake, M. C.; Liu, L.-N. Single-Organelle Quantification Reveals Stoichiometric and Structural Variability of Carboxysomes Dependent on the Environment. *Plant Cell* **2019**, *31* (7), 1648−1664.
(41) Sommer, M.; Cai, F.; Melnicki, M.; Kerfeld, C. A. β-Carboxysome Bioinformatics: Identification and Evolution of New Bacterial Microcompartment Protein Gene Classes and Core Locus Constraints. *J. Exp. Bot.* **2017**, *68* (14), 3841−3855.
(42) Hagen, A.; Sutter, M.; Sloan, N.; Kerfeld, C. A. Programmed Loading and Rapid Purification of Engineered Bacterial Microcompartment Shells. *Nat. Commun.* **2018**, *9* (1), 2881.
(43) Trettel, D. S.; Resager, W.; Ueberheide, B. M.; Jenkins, C. C.; Winkler, W. C. Chemical Probing Provides Insight into the Native Assembly State of a Bacterial Microcompartment. *Structure* **2022**, *30* (4), 537−550.
(44) Jiang, Q.; Li, T.; Yang, J.; Aitchison, C. M.; Huang, J.; Chen, Y.; Huang, F.; Wang, Q.; Cooper, A. I.; Liu, L.-N. Synthetic Engineering of a New Biocatalyst Encapsulating [NiFe]-Hydrogenases for Enhanced Hydrogen Production. *J. Mater. Chem. B* **2023**, *11* (12), 2684−2692.
(45) Nguyen, N. D.; Pulsford, S. B.; Hee, W. Y.; Rae, B. D.; Rourke, L. M.; Price, G. D.; Long, B. M. Towards Engineering a Hybrid Carboxysome. *Photosynth. Res.* **2023**, *156* (2), 265−277.
(46) Kirst, H.; Ferlez, B. H.; Lindner, S. N.; Cotton, C. A. R.; Bar-Even, A.; Kerfeld, C. A. Toward a Glycyl Radical Enzyme Containing Synthetic Bacterial Microcompartment to Produce Pyruvate from Formate and Acetate. *Proc. Natl. Acad. Sci. U. S. A.* **2022**, *119* (8), No. e2116871119.
(47) Li, T.; Jiang, Q.; Huang, J.; Aitchison, C. M.; Huang, F.; Yang, M.; Dykes, G. F.; He, H.-L.; Wang, Q.; Sprick, R. S.; Cooper, A. I.; Liu, L.-N. Reprogramming Bacterial Protein Organelles as a Nanoreactor for Hydrogen Production. *Nat. Commun.* **2020**, *11* (1), 5448.
(48) Wagner, H. J.; Capitain, C. C.; Richter, K.; Nessling, M.; Mampel, J. Engineering Bacterial Microcompartments with Heterologous Enzyme Cargos. *Eng. Life Sci.* **2017**, *17* (1), 36−46.
(49) Lawrence, A. D.; Frank, S.; Newnham, S.; Lee, M. J.; Brown, I. R.; Xue, W.-F.; Rowe, M. L.; Mulvihill, D. P.; Prentice, M. B.; Howard, M. J.; Warren, M. J. Solution Structure of a Bacterial Microcompartment Targeting Peptide and Its Application in the Construction of an Ethanol Bioreactor. *ACS Synth. Biol.* **2014**, *3* (7), 454−465.
(50) Choudhary, S.; Quin, M. B.; Sanders, M. A.; Johnson, E. T.; Schmidt-Dannert, C. Engineered Protein Nano-Compartments for Targeted Enzyme Localization. *PLoS One* **2012**, *7* (3), No. e33342.
(51) Li, T.; Chang, P.; Chen, W.; Shi, Z.; Xue, C.; Dykes, G. F.; Huang, F.; Wang, Q.; Liu, L.-N. Nanoengineering Carboxysome Shells for Protein Cages with Programmable Cargo Targeting. *ACS Nano* **2024**, *18*, 7473.
(52) Lassila, J. K.; Bernstein, S. L.; Kinney, J. N.; Axen, S. D.; Kerfeld, C. A. Assembly of Robust Bacterial Microcompartment Shells Using Building Blocks from an Organelle of Unknown Function. *J. Mol. Biol.* **2014**, *426* (11), 2217−2228.
(53) Ferlez, B.; Sutter, M.; Kerfeld, C. A. A Designed Bacterial Microcompartment Shell with Tunable Composition and Precision Cargo Loading. *Metab. Eng.* **2019**, *54*, 286−291.
(54) Dale, R.; Ohmuro-Matsuyama, Y.; Ueda, H.; Kato, N. Mathematical Model of the Firefly Luciferase Complementation Assay Reveals a Non-Linear Relationship between the Detected Luminescence and the Affinity of the Protein Pair Being Analyzed. *PLoS One* **2016**, *11* (2), No. e0148256.
(55) Dale, R.; Ohmuro-Matsuyama, Y.; Ueda, H.; Kato, N. Non-Steady State Analysis of Enzyme Kinetics in Real Time Elucidates Substrate Association and Dissociation Rates: Demonstration with Analysis of Firefly Luciferase Mutants. *Biochemistry* **2019**, *58* (23), 2695−2702.
(56) Zakeri, B.; Fierer, J. O.; Celik, E.; Chittock, E. C.; Schwarz-Linek, U.; Moy, V. T.; Howarth, M. Peptide Tag Forming a Rapid Covalent Bond to a Protein, through Engineering a Bacterial Adhesin. *Proc. Natl. Acad. Sci. U. S. A.* **2012**, *109* (12), E690−E697.
(57) Ribeiro, C.; Esteves da Silva, J. C. G. Kinetics of Inhibition of Firefly Luciferase by Oxyluciferin and Dehydroluciferyl-Adenylate. *Photochem. Photobiol. Sci.* **2008**, *7* (9), 1085−1090.
(58) Yang, N. J.; Hinner, M. J. Site-Specific Protein Labeling, Methods and Protocols. *Methods Mol. Biol.* **2015**, *1266*, 29−53.
(59) Jakobson, C. M.; Tullman-Ercek, D.; Slininger, M. F.; Mangan, N. M. A Systems-Level Model Reveals That 1,2-Propanediol Utilization Microcompartments Enhance Pathway Flux through Intermediate Sequestration. *PLoS Comput. Biol.* **2017**, *13* (5), No. e1005525.
(60) Long, B. M.; Förster, B.; Pulsford, S. B.; Price, G. D.; Badger, M. R. Rubisco Proton Production Can Drive the Elevation of CO2

https://doi.org/10.1021/acssynbio.4c00290
ACS Synth. Biol. 2025, 14, 1405−1413

within Condensates and Carboxysomes. *Proc. Natl. Acad. Sci. U. S. A.* **2021**, *118* (18), No. e2014406118.
(61) Mangan, N. M.; Flamholz, A.; Hood, R. D.; Milo, R.; Savage, D. F. PH Determines the Energetic Efficiency of the Cyanobacterial CO2 Concentrating Mechanism. *Proc. Natl. Acad. Sci. U. S. A.* **2016**, *113* (36), E5354−E5362.
(62) Vermaas, J. V.; Dixon, R. A.; Chen, F.; Mansfield, S. D.; Boerjan, W.; Ralph, J.; Crowley, M. F.; Beckham, G. T. Passive Membrane Transport of Lignin-Related Compounds. *Proc. Natl. Acad. Sci. U. S. A.* **2019**, *116* (46), 23117−23123.
(63) Branchini, B. R.; Magyar, R. A.; Murtiashaw, M. H.; Anderson, S. M.; Zimmer, M. Site-Directed Mutagenesis of Histidine 245 in Firefly Luciferase: A Proposed Model of the Active Site †. *Biochemistry* **1998**, *37* (44), 15311−15319.
(64) Schenkmayerova, A.; Pinto, G. P.; Toul, M.; Marek, M.; Hernychova, L.; Planas-Iglesias, J.; Liskova, V. D.; Pluskal, D.; Vasina, M.; Emond, S.; Dörr, M.; Chaloupkova, R.; Bednar, D.; Prokop, Z.; Hollfelder, F.; Bornscheuer, U. T.; Damborsky, J. Engineering the Protein Dynamics of an Ancestral Luciferase. *Nat. Commun.* **2021**, *12* (1), 3616.
(65) Melnicki, M. R.; Sutter, M.; Kerfeld, C. A. Evolutionary Relationships among Shell Proteins of Carboxysomes and Metabolosomes. *Curr. Opin. Microbiol.* **2021**, *63*, 1−9.
(66) Du, P.; Xu, S.; Xu, Z.; Wang, Z. Bioinspired Self-Assembling Materials for Modulating Enzyme Functions. *Adv. Funct. Mater.* **2021**, *31* (38), 2104819.
(67) Küchler, A.; Yoshimoto, M.; Luginbühl, S.; Mavelli, F.; Walde, P. Enzymatic Reactions in Confined Environments. *Nat. Nanotechnol.* **2016**, *11* (5), 409−420.
(68) Caparco, A. A.; Dautel, D. R.; Champion, J. A. Protein Mediated Enzyme Immobilization. *Small* **2022**, *18* (19), No. e2106425.
(69) Schindelin, J.; Arganda-Carreras, I.; Frise, E.; Kaynig, V.; Longair, M.; Pietzsch, T.; Preibisch, S.; Rueden, C.; Saalfeld, S.; Schmid, B.; Tinevez, J.-Y.; White, D. J.; Hartenstein, V.; Eliceiri, K.; Tomancak, P.; Cardona, A. Fiji: An Open-Source Platform for Biological-Image Analysis. *Nat. Methods* **2012**, *9* (7), 676−682.
(70) Mirdita, M.; Schütze, K.; Moriwaki, Y.; Heo, L.; Ovchinnikov, S.; Steinegger, M. ColabFold: Making Protein Folding Accessible to All. *Nat. Methods* **2022**, *19* (6), 679−682.
(71) Virtanen, P.; Gommers, R.; Oliphant, T. E.; Haberland, M.; Reddy, T.; Cournapeau, D.; Burovski, E.; Peterson, P.; Weckesser, W.; Bright, J.; van der Walt, S. J.; Brett, M.; Wilson, J.; Millman, K. J.; Mayorov, N.; Nelson, A. R. J.; Jones, E.; Kern, R.; Larson, E.; Carey, C. J.; Polat, İ.; Feng, Y.; Moore, E. W.; VanderPlas, J.; Laxalde, D.; Perktold, J.; Cimrman, R.; Henriksen, I.; Quintero, E. A.; Harris, C. R.; Archibald, A. M.; Ribeiro, A. H.; Pedregosa, F.; van Mulbregt, P.; Contributors, S.; Vijaykumar, A.; Bardelli, A. P.; Rothberg, A.; Hilboll, A.; Kloeckner, A.; Scopatz, A.; Lee, A.; Rokem, A.; Woods, C. N.; Fulton, C.; Masson, C.; Häggström, C.; Fitzgerald, C.; Nicholson, D. A.; Hagen, D. R.; Pasechnik, D. V.; Olivetti, E.; Martin, E.; Wieser, E.; Silva, F.; Lenders, F.; Wilhelm, F.; Young, G.; Price, G. A.; Ingold, G.-L.; Allen, G. E.; Lee, G. R.; Audren, H.; Probst, I.; Dietrich, J. P.; Silterra, J.; Webber, J. T.; Slavič, J.; Nothman, J.; Buchner, J.; Kulick, J.; Schönberger, J. L.; Cardoso, J. V. de M.; Reimer, J.; Harrington, J.; Rodríguez, J. L. C.; Nunez-Iglesias, J.; Kuczynski, J.; Tritz, K.; Thoma, M.; Newville, M.; Kümmerer, M.; Bolingbroke, M.; Tartre, M.; Pak, M.; Smith, N. J.; Nowaczyk, N.; Shebanov, N.; Pavlyk, O.; Brodtkorb, P. A.; Lee, P.; McGibbon, R. T.; Feldbauer, R.; Lewis, S.; Tygier, S.; Sievert, S.; Vigna, S.; Peterson, S.; More, S.; Pudlik, T.; Oshima, T.; Pingel, T. J.; Robitaille, T. P.; Spura, T.; Jones, T. R.; Cera, T.; Leslie, T.; Zito, T.; Krauss, T.; Upadhyay, U.; Halchenko, Y. O.; Vázquez-Baeza, Y. SciPy 1.0: Fundamental Algorithms for Scientific Computing in Python. *Nat. Methods* **2020**, *17* (3), 261−272.
(72) Marquardt, D. W. An Algorithm for Least-Squares Estimation of Nonlinear Parameters. *J. Soc. Ind. Appl. Math.* **1963**, *11* (2), 431−441.

https://doi.org/10.1021/acssynbio.4c00290
ACS Synth. Biol. 2025, 14, 1405−1413